INT. J. NUM. METH. HEAT FLUID FLOW, VOL. 4, 347–365 (1994)

NUMERICAL COMPUTATION OF LAMINAR FLOW IN A HEATED ROTATING CAVITY WITH AN AXIAL THROUGHFLOW OF AIR

C. A. LONG† AND P. G. TUCKER‡

† *Thermo-Fluid Mechanics Research Centre, School of Engineering, University of Sussex, Brighton, Sussex BN1 9QT, UK*
‡ *School of Mechanical Engineering, University of Bath, Bath, BA2 7AY, U.K.*

ABSTRACT

A heated rotating cavity with an axial throughflow of cooling air is used as a model for the flow in the cylindrical cavities between adjacent discs of a high-pressure gas-turbine compressor. In an engine the flow is expected to be turbulent, the limitations of this laminar study are fully realised but it is considered an essential step to understand the fundamental nature of the flow. The three-dimensional, time-dependent governing equations are solved using a code based on the finite volume technique and a multigrid algorithm. The computed flow structure shows that flow enters the cavity in one or more radial arms and then forms regions of cyclonic and anticyclonic circulation. This basic flow structure is consistent with existing experimental evidence obtained from flow visualization. The flow structure also undergoes cyclic changes with time. For example, a single radial arm, and pair of recirculation regions can commute to two radial arms and two pairs of recirculation regions and then revert back to one. The flow structure inside the cavity is found to be heavily influenced by the radial distribution of surface temperature imposed on the discs. As the radial location of the maximum disc temperature moves radially outward, this appears to increase the number of radial arms and pairs of recirculation regions (from one to three for the distributions considered here). If the peripheral shroud is also heated there appear to be many radial arms which exchange fluid with a strong cyclonic flow adjacent to the shroud. One surface temperature distribution is studied in detail and profiles of the relative tangential and radial velocities are presented. The disc heat transfer is also found to be influenced by the disc surface temperature distribution. It is also found that the computed Nusselt numbers are in reasonable accord over most of the disc surface with a correlation found from previous experimental measurements.

KEY WORDS Axial throughflow Multigrid Rotating flow Rotationally-induced buoyancy Three-dimensional and time-dependent numerical computation

NOMENCLATURE

a, b	inner and outer radius of cavity,	k	thermal conductivity,
		L	characteristic length,
A, A_0, A_1	coefficients,	m	coolant mass flow rate,
c	correction,	n	normal to a surface,
C	chemical species,	np	number of planes in which grid is coarsened,
C_p	constant-pressure specific heat,	$Nu = qL/\Delta Tk$	local Nusselt number
D	deficit or residual,	$p = P - \rho\Omega^2 r^2/2$	reduced static pressure,
$E = \Omega^2 r^2/2C_p\Delta T$	Eckert number,	P	static pressure,
$G = s/b$	cavity gap ratio,	$Pr = \mu C_p/k$	Prandtl number,
$Gr = \Omega^2 r\beta\Delta T L^3/\nu^2$	rotational Grashof number,	q	heat flux,

0961–5539/94/040347–20$2.00

Received February 1993
Revised November 1993

r, z, θ radial, axial and tangential coordinates,
R characteristic gas constant,
$Re_z = 2Wa/\nu$ axial Reynolds number,
$Re_\phi = \Omega b^2/\nu$ rotational Reynolds number
$Ro = W/\Omega a$ Rossby number,
s axial gap between the discs,
S source term,
$Sc = \nu/\Gamma$ Schmidt number,
t time,
T static temperature,
u, v, w radial, tangential and axial velocity components in a coordinate system rotating at Ω rad/sec,
W bulk average velocity at cavity inlet.

Greek

α_0, α_1 Gosman relaxation terms,
$\beta = 1/T$ volume expansion coefficient,
Δt time-step length,
ΔT temperature difference,
Γ diffusion coefficient,
$\lambda = 2\mu/3$ viscosity coefficient,
ν kinematic viscosity,
μ dynamic viscosity,
ρ density,
ϕ generalized transport variable,
ω circumferentially-averaged rotational speed of fluid core between the discs,
Ω rotational speed of the discs.

Subscripts

cav pertaining to inside the cavity,
i pertaining to the cavity inlet,
m denotes grid level,
new, old pertaining to new and old values, respectively,
p grid point under consideration,
r, z, θ pertaining to radial, axial and tangential components,
ref appropriate reference value,
s pertaining to the disc surface
u, v, w, T pertaining to the variables u, v, w and T,
ϕ pertaining to the generalized transport variable.

Superscripts

f originating from a fine mesh,
approximate solution.

INTRODUCTION

In modern aero-engine gas turbines, it is common practice to supply cooling air to the turbine discs and blades. This cooling air is bled from successive compressor stages and then flows axially between the bores of adjacent discs in the high-pressure compressor. A schematic diagram showing a cross-sectional view through a typical high-pressure compressor and the associated cooling flows is shown in *Figure 1*. Some of the central axial throughflow enters the cavities formed between the adjacent discs and a parasitic temperature rise occurs in the throughflow air as a result of the convective heat transfer. A knowledge of the heat transfer in these compressor cavities is important for two reasons. First, the engine designer obviously needs to know the temperature of the turbine cooling air, and secondly to calculate the disc temperatures in order to predict the stress and radial growth.

A simplified version of the above comprises a cylindrical cavity (formed by two discs of outer radius, b and a peripheral shroud of axial width, s) which rotates with an angular velocity, Ω. The central throughflow enters the cavity, with a bulk average velocity in the axial direction of W, through a hole of radius a, in the upstream disc and leaves via an identical hole in the downstream disc. An experimental study of the flow structure and heat transfer for the case when the discs are heated was reported by Farthing *et al.*[1,2]. The essential features of the observed

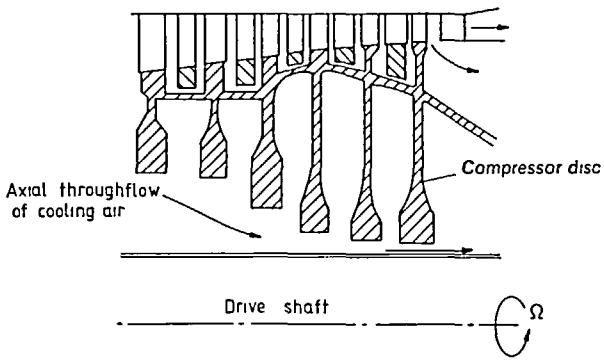

Figure 1 Simplified arrangement of a high pressure compressor drum

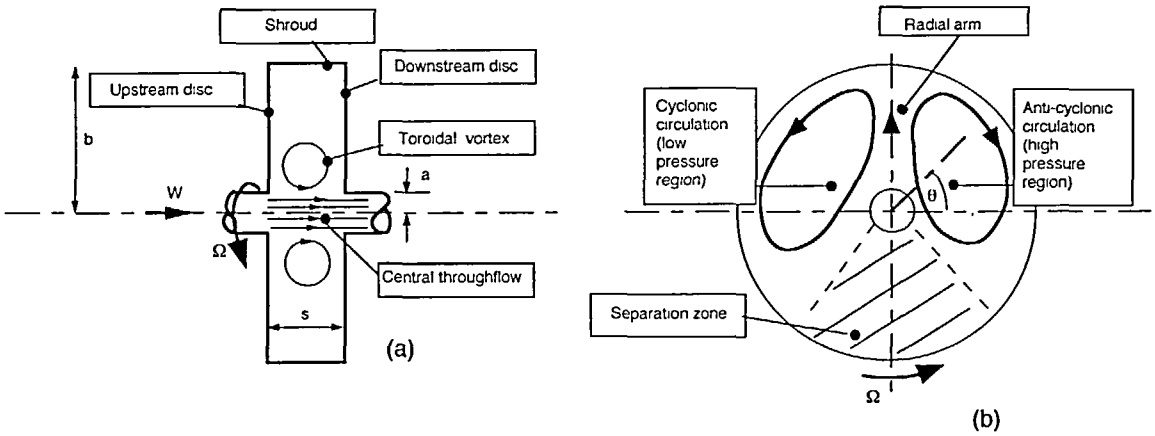

Figure 2 Schematic diagrams of flow in a rotating cavity with an axial throughflow. (a) Isothermal flow, $T_s = T_i$ (r–z plane) and (b) heated flow, $T_s > T_i$ (r–θ plane)

flow structure are illustrated in *Figure 2*. When the discs are unheated, the flow structure is similar to that shown in *Figure 2a*. In this case the central jet passing through the cavity (the throughflow) generates a toroidal vortex. In the absence of various modes of isothermal vortex breakdown (see Farthing *et al.*), the flow is two-dimensional and there is virtually no penetration of the throughflow into the cavity itself.

When the discs are heated, there is a dramatic change in the flow structure: it becomes three-dimensional and time-dependent. Some of the central throughflow now enters the cavity as a result of buoyancy effects which are themselves induced by rotation. The following description is based on observations of the flow in a cavity with a surface temperature distribution that decreases with radius. It was found that this gave a clearly defined flow pattern; for a surface temperature distribution that increases with radius, flow still enters the cavity but the features of the flow cannot be clearly identified. A schematic of the heated flow structure, given in the r–θ plane as this best illustrates the relevant features, is shown in *Figure 2b*. In the region between the two discs, the flow now comprises: a radial arm and a pair of circulation regions. Multiples of this basic flow structure have also been observed, i.e. two radial arms and two pairs of circulations etc. This entire flow rotates at an average angular velocity ω, which is found

to vary with gap ratio, Rossby number ($W/\Omega a$) and thermal conditions, but typically $0.9 < \omega/\Omega < 1$. Fluid in the radial arm enters the cavity, bifurcates at the shroud and forms the regions of circulation. The cyclonic region rotates in the same direction as the discs; the anticyclonic region, in the opposite direction. Under most conditions the regions of circulation do not merge but are observed to be separated by a region which fluid does not enter. Because the circulations rotate in opposite directions they are at different pressures; and just as their meteorological equivalents, the cyclonic region has a lower pressure than the anticyclonic region. The consequence of this is best demonstrated by considering the linear tangential momentum equation in a rotating frame of reference. For steady, incompressible and inviscid flow, this simplifies to:

$$2\Omega u = -1/\rho r(\partial p/\partial \theta) \tag{1}$$

where r and θ are the respective radial and tangential coordinates, p is the reduced static pressure, ρ is the density and u is the radial velocity.

It is evident from inspection of (1) that there can only be a radial flow (in this case u) in the inviscid region between the discs if there is a circumferential variation of pressure: which of course is provided by a cyclone and anticyclone pair. Inspection of *Figure 2b* also reveals that, in the radial arm, $\partial p/\partial \theta < 0$ and from (1), $u > 0$; so radial outflow occurs. Conversely, away from the radial arm and between a pair of circulation regions, $\partial p/\partial \theta > 0$ and so radial inflow may be expected to occur.

Farthing *et al.*[1] also correlated the heat transfer from the discs and found this to depend on both the Reynolds number of the axial throughflow, Re_z, ($Re_z = 2aW/\nu$ where ν is the kinematic viscosity) and the rotational Grashof number, Gr ($Gr = \Omega^2 r\beta\Delta T L^3/\nu^2$ where $\beta\Delta T$ is a buoyancy parameter). One particularly significant finding was that the appropriate characteristic length for the Nusselt and Grashof numbers, L, was the distance measured radially inward from the shroud; implying that a boundary layer flows in this direction. They also correlated the measured local disc surface Nusselt numbers, Nu, with the local Grashof number, Gr, and found that $Nu \propto Gr^{1/4}$ a relation usually associated with laminar flow in natural convection.

Although the experimental work has been relatively successful, there has to date been no successful numerical modelling of this complex flow. It is this topic which forms the subject of this paper. It is also hoped that the work presented will also be of use as a 'test case' for other CFD codes which model three-dimensional, time-dependent flows involving buoyancy and rotation. A full study involving the various effects of rotational speed, flow rate etc. has not been considered here and it is hoped this will be reported in a future paper. The governing equations of conservation of mass, momentum and energy are solved using a finite volume technique and a multigrid algorithm; these details will be presented in the next two sections. The results of the computations are presented and some comparisons with flow visualization are made later.

GOVERNING EQUATIONS

Equations of motion

A schematic diagram of the numerical model and boundary conditions for this flow configuration is shown in *Figure 3*. At radial, tangential and axial coordinates, r, θ, z, the fluid has radial, tangential and axial components of velocity (relative to a coordinate system rotating at the same speed as the cavity) u, v and w, respectively. The absolute static temperature, static pressure, specific heat at constant pressure, thermal conductivity and dynamic viscosity of this fluid are T, P, C_p, k and μ, respectively.

For the flow considered here, the Eckert number, $E = \Omega^2 r^2/2C_p\Delta T$ (where ΔT is the temperature difference between the incoming air and the maximum value on the disc surface), is small ($E < 4 \times 10^{-5}$). So compressive heating in the energy equation will be neglected. Relative to the discs, the flow structure of the cavity is slow moving, because $\omega \simeq \Omega$, so the terms in the

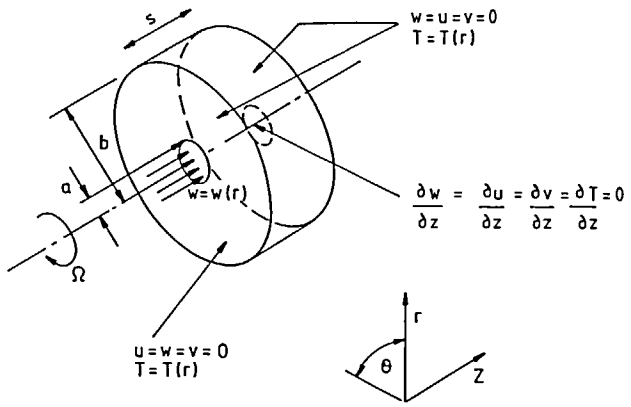

Figure 3 Schematic diagram of the numerical model and boundary conditions

Table 1 Diffusion coefficients for the generalized transport equation (2)

ϕ	$\Gamma_{\phi,z}$	$\Gamma_{\phi,r}$	$\Gamma_{\phi,\theta}$
w	$2\mu + \lambda$	μ	μ
u	μ	$2\mu + \lambda$	μ
v	μ	μ	$2\mu + \lambda$
T	k/Cp	k/Cp	k/Cp

energy equation associated with viscous dissipation can also be ignored. The variation of density with pressure is calculated using the equation of state, $\rho = P/\mathbf{R}T$, where $\mathbf{R}$ is the characteristic gas constant.

The time-dependent equations describing the conservation of momentum and energy in three dimensions for a compressible fluid, with variable dynamic viscosity, in a rotating coordinate system, are stated in a common form for the general transport variable ϕ, by:

$$\partial(\rho\phi)/\partial t + \partial(\rho w\phi)/\partial z + r^{-1}\partial(\rho ru\phi)/\partial r + r^{-1}\partial(\rho v\phi)/\partial\theta = \partial((\Gamma_{\phi,z})\partial\phi/\partial z)/\partial z + r^{-1}\partial((\Gamma_{\phi,r})r\partial\phi/\partial r)/\partial r + r^{-1}\partial(r^{-1}\Gamma_{\phi,\theta}\partial\phi/\partial\theta)/\partial\theta) + S_\phi \quad (2)$$

The diffusion coefficients, Γ_ϕ for (2) are given in *Table 1*, where $\lambda = -2\mu/3$, and the subscripts z, r and θ denote the respective components in the axial, radial and tangential directions.

The source terms, S_ϕ, when $\phi = w, u, v, T$ are as follows:

$$S_w = -\partial p/\partial z + \partial(\lambda r^{-1}\partial(ru)/\partial r)/\partial z + \partial(\lambda r^{-1}\partial v/\partial\theta)/\partial z + r^{-1}\partial(\mu r\partial u/\partial z)/\partial r + r^{-1}\partial(\mu\partial v/\partial z)/\partial\theta$$

$$S_u = -\partial p/\partial r + \partial(\mu\partial w/\partial r)/\partial z + \partial(\lambda\partial w/\partial z)/\partial r + \partial(\lambda r^{-1}\partial v/\partial\theta)/\partial r + r^{-1}\partial(\mu r\partial(vr^{-1})/\partial r)/\partial\theta - r^{-2}2\mu(\partial v/\partial\theta) + 2\rho v\Omega + u\partial(\lambda r^{-1})/\partial r - 2\mu u/r^2 + \rho v^2/r$$

$$S_v = -r^{-1}\partial p/\partial\theta - \rho uvr^{-1} - \mu vr^{-2} - vr^{-1}\partial\mu/\partial r + \partial(\mu r^{-1}\partial w/\partial\theta)/\partial z + r^{-2}\partial(\mu r\partial u/\partial\theta)\partial r + r^{-1}\partial(\lambda\partial w/\partial z)\partial\theta + r^{-1}\partial(\lambda r^{-1}\partial(ru)/\partial r)/\partial\theta + r^{-1}\partial(2\mu ur^{-1})/\partial\theta - 2\rho u\Omega$$

$$S_T = 0$$

The continuity equation for time-dependent flow of a compressible fluid is given by:

$$\partial\rho/\partial t + \partial(\rho w)/\partial z + r^{-1}\partial(\rho ur)/\partial r + r^{-1}\partial(\rho v)/\partial\theta = 0 \quad (3)$$

Initial and boundary conditions

At time $t = 0$, the initial conditions for the variables u, v, w, p, T and ρ inside the cavity (i.e., for $0 \leqslant r \leqslant b$, $0 < \theta \leqslant 2\pi$ and $0 \leqslant z \leqslant s$) are:

$$u = v = w = 0 \qquad p = 1.03 \times 10^5 \text{ Pa} \qquad T = T_i \qquad \rho = P/\mathbf{R}T_i$$

Various tests were carried out to verify that the solutions were independent of the chosen initial conditions (notably different initial tangential velocity distributions). The results presented in this paper are considered to be virtually independent of the initial conditions.

For $t > 0$, the disc and shroud surface temperatures are specified (the precise form will be stated as appropriate later in the paper) and on these boundaries $u = v = w = 0$. At the cavity inlet (i.e., $z = 0$, $r \leqslant a$ and for $0 < \theta \leqslant 2\pi$) $T = T_i$, $u = v = 0$; and either $w = (Re_z v/2a) = W$ (a constant velocity profile) or $w = 2W(1 - (r/a)^2)$ (a parabolic velocity profile). At the cavity outlet ($z = s$, $r \leqslant a$ and for $0 < \theta \leqslant 2\pi$), $\partial\phi/\partial z = 0$, where $\phi = u$, v, w or T.

Experimental evidence of Farthing *et al.*[2] suggests that for the Rossby number considered here ($Ro = 8$) the flow at the cavity exit is parabolic (i.e. not influenced by the downstream flow conditions). For lower values of Rossby number $Ro \approx 1$, the experimental evidence shows that the exit flow is not parabolic; there is flow reversal and the numerical predictions of Tucker[3] (which are not presented here) show this. This would suggest that the chosen boundary conditions are satisfactory. However, further tests were performed to check the sensitivity of solutions to the downstream boundary conditions. These involved selectively changing different differential boundary conditions at the cavity outlet to Dirichlet (matching those at the cavity inlet). Also, different pressure distributions at the cavity outlet were tested. The pressure distribution was assumed to be either uniform and at atmospheric pressure or a parabolic distribution (based on the swirl velocity at the cavity outlet). These tests revealed the solutions were insensitive to the cavity exit boundary conditions.

Numerical modelling of the flow visualization results

The governing equation for the transport of a species, of mass concentration, C is:

$$\partial C/\partial t + w\partial C/\partial z + u\partial C/\partial r + vr^{-1}\partial C/\partial\theta = \Gamma[\partial(\partial C/\partial z)/\partial z + r^{-1}\partial(r\partial C/\partial r)/\partial r + r^{-2}\partial(\partial C/\partial\theta)/\partial\theta] \quad (4)$$

Equation (4) was solved using a time-step of $\Delta t = 1$ sec and with the following initial condition at $t = 0$:

for $0 \leqslant r \leqslant b; 0 \leqslant z/s \leqslant 1; 0 < \theta \leqslant 2\pi, C = 0$ and the following boundary conditions for $t > 0$:

(i) for the cavity inlet ($z = 0$, $r \leqslant a$ and $0 < \theta \leqslant 2\pi$), $C = 100$;
(ii) for the cavity outlet ($z = s$, $r \leqslant a$ and $0 < \theta \leqslant 2\pi$), $\partial C/\partial n = 0$, where n is the appropriate outward normal;
(iii) for the disc surfaces and shroud ($z = 0$, $a < r \leqslant b$ and $0 < \theta \leqslant 2\pi$; $z = s$, $a < r \leqslant b$ and $0 < \theta \leqslant 2\pi$ and $0 \leqslant z \leqslant s$, $r = b$ and $0 < \theta \leqslant 2\pi$), $\partial C/\partial n = 0$, where n is the appropriate normal.

SOLUTION METHOD

Discretization scheme

The equations of motion are discretized using the control volume formulation described by Patankar[4], and an implicit time scheme was used. The grids used in the momentum equations are staggered as shown in *Figure 4*, and the computational advantages of this are discussed in the book by Patankar. The hybrid scheme of Spalding[5] is used to interpolate

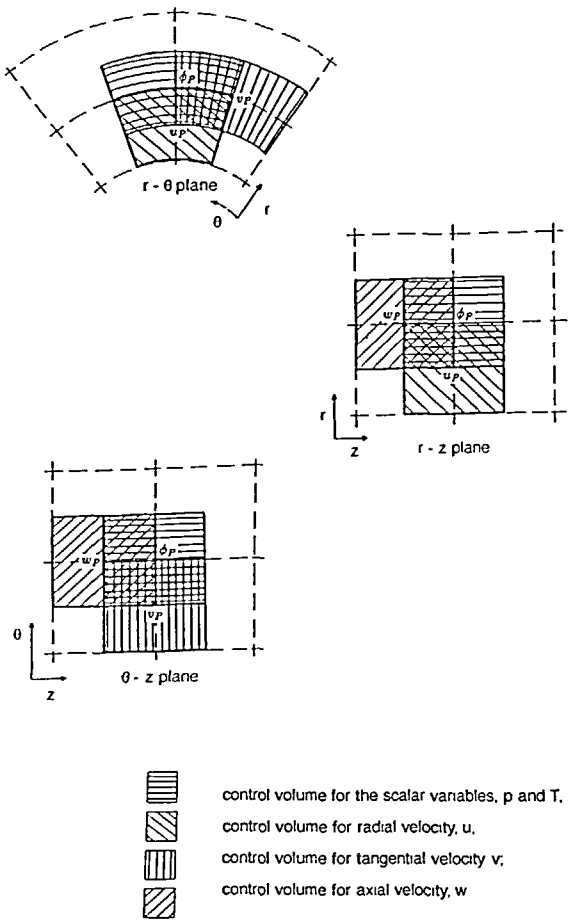

Figure 4 Relative location of control volumes

variables from the main grid points onto the finite control volume faces. The pressure field over the region is obtained from the continuity equation using the SIMPLEC method of Van Doormal and Raithby[6].

The choice of coordinate system is found to have a significant influence on the solutions. Relative to a stationary coordinate system, the flow has a large tangential velocity since $v \approx \Omega r$. The control-volume Peclet number (for the momentum equation, this is equivalent to a Reynolds number defined using local velocity, grid size and kinematic viscosity) will usually exceed a value of 2, at which a second-order central difference scheme becomes unstable, and the hybrid scheme used switches over to the more stable upwind difference scheme. However, this has two disadvantages: the accuracy is limited to first-order and, the increased stability can damp the tangential variations of variables leading to an axisymmetric solution. The Peclet number can be reduced by either reducing the grid size or adopting a coordinate system rotating at the cavity speed, Ω. Since the former requires more overall computing resources, the latter choice is preferable, and is used for all the results discussed here.

The dominant terms in the radial momentum equation are the radial pressure gradient and the centrifugal force term, which involves tangential velocity. This leads to strong coupling which

can create difficulties with convergence. Gosman *et al.*[7] proposed use of the term: $\alpha_0 \rho |v + \alpha_1 \Omega r|(u_{old} - u_{new})/r$, where α_0 and α_1 are the Gosman relaxation terms and the subscripts 'old' and 'new' denote values at the previous and current iterations. This is added to the source term in the radial momentum equation to improve convergence, and in its original formulation $\alpha_1 = 1$. Use of these Gosman relaxation terms was found by Vaughan[8] to be highly effective in improving the speed of convergence when solving axisymmetric rotating flows. This use is continued in the current three-dimensional predictions.

The multigrid algorithm

The speed, with which the discretized equations can be solved, is increased by the use of a non-linear multigrid algorithm. The axisymmetric version is discussed in detail by Vaughan *et al.*[9]. A three-dimensional version is used here which includes some minor improvements, and so a brief discussion is considered appropriate.

A differential equation in the discretized form $[A][\phi] = [S]$, is represented on a fine mesh, denoted by use of the subscript m. If ϕ'_m is the approximate solution to ϕ_m and c_m, the correction to complete the solution on the fine mesh then:

$$[A_m][(\phi'_m + c_m)] = S_m \tag{6}$$

The residual or deficit D, is defined as:

$$[D_m] = [S_m] - [A_m][\phi'_m] \tag{7}$$

Combining (6) and (7) gives,

$$[A_m][(\phi'_m + c_m)] = [D_m] + [A_m][\phi'_m] \tag{8}$$

For a more coarse mesh, denoted by the subscript $m + 1$, (8) is rewritten as:

$$[A_{m+1}][(\phi'^{f}_{m+1} + c_{m+1})] = [D^{f}_{m+1}] + [A_{m+1}][(\phi'^{f}_{m+1})] \tag{9}$$

where the superscript f indicates that the value originates from the finer mesh. This process is in fact referred to as restriction; a weighted operator is used to transpose the variables from the fine grid to the coarse grid. For the main (as opposed to staggered) grid variables, which are temperature and pressure the number of points used in the restriction for a three-dimensional problem is 3^{np} where np is the number of planes in which the grid is made more coarse (i.e., a 27 point restriction is used when the grid is coarsened in all three planes). For the staggered grid variables (i.e. the velocity components) the number of points used in the restriction is $2(3^{np-1})$.

Equation (9) can be represented on successively coarser meshes. In the work discussed here three meshes were used in a so-called V-cycle. For a V-cycle, (9) is solved for corrections c_m and c_{m+1} to the variables, represented here by ϕ, on successively coarser grids. Once the coarsest grid has been reached the corrections are interpolated onto the next finest grid and so on. In this way, two solutions to (9) are obtained at each grid level.

Grid coarsening, on the $m + 1$ grid level for example, is normally achieved by missing out alternate main grid nodes on grid level m, in the axial, radial and tangential directions. But for the work presented here, grid coarsening for each plane was controlled independently. This feature allows the aspect ratio of the coarse grids to be controlled. The three-dimensional, time-dependent problems which are the main subject of this paper use considerable CPU time (for $\Delta t = 0.05$ sec, approximately 900 sec per time-step on a Solbourne 5E/905-128 mainframe and about 130 sec per time-step when using a Cray XMP/48). Consequently, it was not possible to investigate the effect of using different aspect ratios for the restricted (coarse) grids in three-dimensional geometries. Some preliminary investigations were, however, applied to axisymmetric problems of the flow between a rotating and stationary disc (rotor–stator) problems. The results from this work suggest that the choice of coarse grid aspect ratio can effect a 10% saving in CPU time.

The multigrid algorithm employed three grid levels in the axial, radial and circumferential directions. On the finest and intermediate grid levels, 2 relaxation sweeps each involving 6 pressure correction sweeps were used. For the coarsest grid, 3 relaxation sweeps each involving 6 pressure correction sweeps were used.

Convergence criteria

The parameters used to monitor convergence were the normalized residuals and also the root-mean square (rms) change in all the variables. The latter is defined as, $\text{rms}_\phi = (\sum (\phi_{\text{new}} - \phi_{\text{old}})^2 / [\sum (\phi_{\text{new}})^2])^{1/2}$, where the summation applies over the entire solution domain. At the end of a time-step, the value of rms_ϕ was below 5×10^{-5} (but, typically an order of magnitude smaller than this). The residuals for the axial, radial and tangential momentum equations are normalized using $\rho u_{\text{ref}}^2 \pi b s/2$, where u_{ref} is the maximum radial velocity at $r = b/2$ and $z = s/2$. The residual of the pressure correction equation is made dimensionless by dividing by the new mass flow rate of fluid actually entering the cavity (typically 1 to 2% of the throughflow flow rate), m_{cav}. For the energy equation, the product of flow rate entering the cavity and the maximum temperature difference between the cavity walls and the incoming air is used to normalize the residuals. These (u_{ref} and m_{cav}) normalizing parameters are chosen in preference to the perhaps more obvious choice of bulk axial velocity W, and total throughflow rate m, since they are considered to be more appropriate. Use of the latter can bring about a relaxation in the convergence criteria with the result that insufficiently converged solutions can be obtained. After 5 sec, the maximum of the normalized residuals for all the equations is less than 2×10^{-2}, a typical average value is 0.75×10^{-2}.

RESULTS AND DISCUSSION

Test case details

The test case to be discussed used a $17 \times 21 \times 40$ grid (in the axial, radial and tangential directions, respectively) with $\alpha_0 = \alpha_1 = 2$ and a time-step of $\Delta t = 0.05$ sec. Although relatively coarse, the grid was chosen due to limitations in CPU time and storage requirement. However, solutions made with a $33 \times 33 \times 60$ grid on the CRAY XMP/48 and also a second-order convective term treatment suggest reasonable grid-independence of most solutions presented here. The dependence of the solutions on the time-step length was investigated and it was found that the results became time-step independent for $\Delta t < 0.2$ sec.

The results focus on a single geometry: $a = 0.0108$ m, $b = 0.108$ m and $s = 0.0288$ m, giving $a/b = 0.1$ and $G = s/b = 0.267$ (see *Figure 3*). These dimensions were chosen as they correspond to the apparatus used in most of the experimental flow visualization work by Farthing *et al.*[2]. The numerical results were obtained for a constant value of the axial and rotational Reynolds numbers: $Re_z = 2180$ and $Re_\phi = 1.3 \times 10^4$, again corresponding to a condition where there is available experimental evidence. The emphasis of this paper is to report on the development of a technique, and consequently a systematic investigation of the effects of axial and rotational Reynolds numbers will not be presented here (it is hoped to address these topics in a future paper). Both discs are heated with the same axisymmetric surface temperature distribution, and four different temperature distributions were investigated. These are illustrated in *Figure 5*, frames (a), (b), (c) and (d), and will be referred to as temperature distributions A, B, C, and D, respectively. Temperature distribution A, decreases with radius and is defined by:

$$T_s = A_0 + A_1 r/b \tag{10}$$

where $A_0 = 382$ K and $A_1 = -89$ K; at the shroud the surface temperature is 293 K. The other temperature distributions are defined by two such similar expressions blended by a smooth curve

in the region where they intersect. The coefficients for (10), and the radial extent for which these apply, for each temperature distribution are listed in *Table 2*.

It is believed that the disc surface temperature distributions used in the experimental flow visualization work of Farthing *et al.*[2], were similar to distributions A and B. At inlet to the cavity the air has a temperature of $T_i = 293$ K.

Validation tests cases

Several test cases were chosen to validate different aspects of the code. Full details of this work are available in Tucker[3], so only a brief outline of it is given here. Three-dimensional, buoyancy-induced, steady state solutions in a stationary cylinder were validated by comparison with numerical predictions by Bontoux *et al.*[10] and experimental measurements of Schiroky and Rosenberger[11]. Excellent (usually better than 1%) agreement was obtained between the numerical predictions of velocity distributions. Time-dependent, 3-D, buoyancy-induced solutions were obtained for the flow investigated by Castrejon and Spalding[12]. Although these authors did not publish any quantitative data, acceptable agreement was obtained between predictions of the flow structure showing the time-dependent growth of the buoyant plume. For the above two test cases, the flows are in a non-rotating container. The results of Hide[13] and Hignett *et al.*[14]

Table 2 Coefficients of (10) describing the four disc surface temperature distributions investigated

Temperature distribution	Inner curve	A_0 (K)	A_1 (K)	Outer curve	A_0 (K)	A_1 (K)
A	none	—	—	$0.1 \leqslant r/b \leqslant 1$	382	−89
B	$0.1 \leqslant r/b \leqslant 0.263$	277	309	$0.263 \leqslant r/b \leqslant 1$	382	−89
C	$0.1 \leqslant r/b \leqslant 0.492$	298	122	$0.492 < r/b \leqslant 1$	420	−127
D	$0.1 \leqslant r/b \leqslant 0.768$	300	75	$0.768 < r/b \leqslant 1$	573	−280

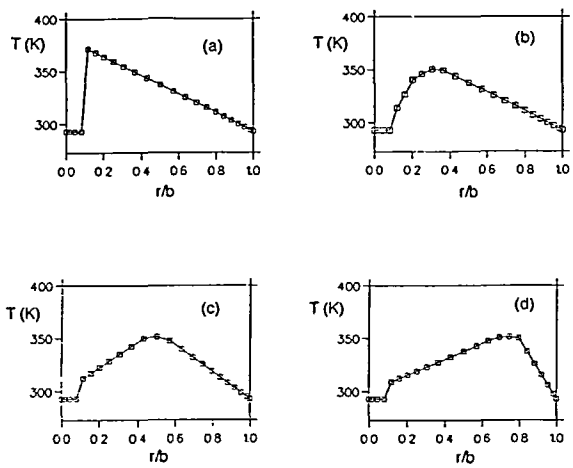

Figure 5 The different disc surface temperature distributions investigated (see (10) and *Table 2*). (a) Distribution A; (b) distribution B; (c) distribution C; (d) distribution D

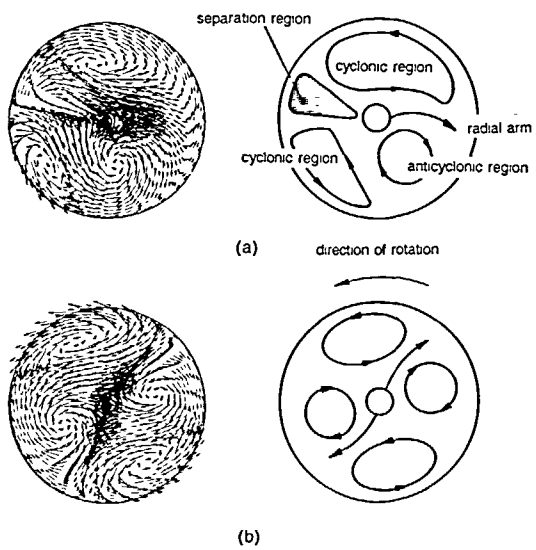

Figure 6 Computed velocity vectors and schematic diagrams of the flow in the mid-axial ($z = s/2$), r–θ plane with: $\Delta t = 0.05$ sec; temperature distribution A; $Re_\phi = 1.3 \times 10^4$ and $Re_z = 2180$. (a) $t = 31.5$ sec and (b) $t = 42$ sec

were used to validate a 3-D test case involving the combined effects of rotation, buoyancy and time-dependence. No velocity measurements were published by Hide, but good qualitative agreement was obtained; in terms of a non-dimensional characterizing parameter the current program was able to predict the observed flow pattern. White[15] believes that at $t = 250$ sec, this particular flow should reach a cyclic form of time dependence. But Hignett *et al.* published their predicted and measured velocity data for $t = 1000$ sec. Due to limitations in computing budget it was not possible to obtain solutions at this time, and since one objective of their study was to study the vacillations which occur over this time scale it was also considered unnecessary. Comparisons between the tangential velocity distributions and wave number obtained from the two sets of numerical results at $t = 250$ sec and 1000 sec, and experimental measurements gave generally good agreement. In some cases the current predictions agreed more favourably with the experimental measurements of Hignet *et al.* than their own predictions.

The basic flow structure

The essential features of the flow structure at $t = 31.5$ and 42 sec for disc surface temperature distribution A are illustrated in *Figure 6*. On the left-side of the figure are the computed velocity vectors at $z/s = 0.5$ obtained from solutions with $\Delta t = 0.05$ sec, and on the right-side are schematic diagrams of the flow. The cavity is rotating in an anticlockwise sense.

Although not shown here, the basic flow structure becomes established at $t = 6$ sec and for times greater than this the flow exhibits a cyclic form of time-dependence, i.e., changes in the flow structure occur as time progresses and these changes are repeated in a cycle. The vector plot at $t = 31.5$ sec, shows flow to enter the cavity in a radial arm (seen in approximately the 3 o'clock position). The region of flow above the radial arm rotates with the sense of rotation of the cavity. This is a cyclonic region, there being another cyclonic region at approximately 7 o'clock. The region below the radial arm (at approximately 5 o'clock) rotates against the cavity; this is the anticyclonic region. Opposite the radial arm and between the two cyclonic regions, is a region showing characteristics of the separation zone, which forms from an earlier anticyclonic region. At $t = 42$ sec (frame (b)), there are now two radial arms (at 2 o'clock and 8 o'clock), two regions of cyclonic flow and two smaller regions of anticyclonic flow. Although not shown here, where there are regions of cyclonic flow the fluid moves axially away from the disc surface. For regions of anticyclonic flow, fluid moves axially (or is entrained) towards the disc surface. This finding is consistent with the behaviour of surface flows and the analogous meterological phenomena.

The effect of the disc surface temperature distribution on the computed flow structure is shown in *Figure 7*. Frames (a), (b), (c) and (d) show the velocity vectors in the mid-axial plane ($z = s/2$) corresponding to surface temperature distributions A (at $t = 60$ sec), B (at $t = 30.9$ sec), C (at $t = 33$ sec) and D (at $t = 59$ sec), respectively. In all these cases the periphery of the cavity (or shroud) is at $T = T_i$ ($= 293$ K). In frame (e) the shroud is also heated, to the maximum disc surface temperature of 353 K this computation was started using the results shown in frame (d) for the initial conditions and allowed to run until $t = 88.6$ sec. As was shown in *Figure 6* for temperature distribution A, the flow structure changes from one characterized by a single radial arm, cyclone, anticyclone and a separation zone to two radial arms, two cyclones and two anticyclones and then back again. Analysis of the flow structure has concluded that although the flow cycles in this manner, the predominant flow structure is that with the single radial arm; this is shown in *Figure 7a*. For disc surface temperature distribution B, the flow structure always has two radial arms, two cyclones, two anticyclones and no separation zone. This flow structure is shown in frame (b). A similar (two-armed) flow structure occurs with temperature distribution C, there being only a few differences in detail between this and temperature distribution B. Shifting the location of the maximum disc surface temperature towards the outer radius, as in distribution D, creates a significant difference in the flow structure (see frame (d)). It is now difficult to distinguish radial arms, cyclones and anticyclones. There appears to be a strong

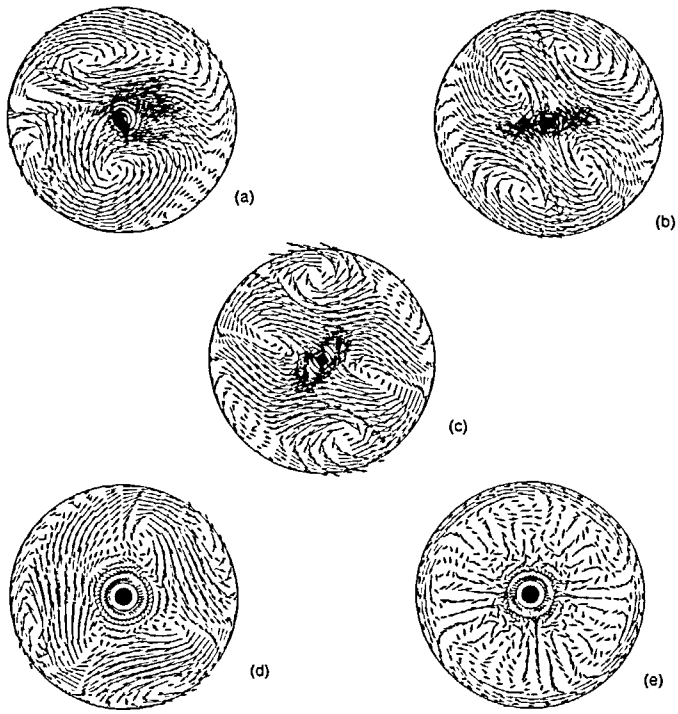

Figure 7 Computed velocity vectors in the mid-axial ($z = s/2$), r–θ plane for different disc surface temperature distributions, $\Delta t = 0.05$ sec, $Re_\phi = 1.3 \times 10^4$ and $Re_z = 2180$. (a) Distribution A, $t = 60$ sec; (b) distribution B, $t = 30.9$ sec; (c) distribution C, $t = 33$ sec; (d) distribution D, $t = 59$ sec; (e) distribution D and a heated shroud, $t = 88.6$ sec

anticyclonic flow over most of the cavity, three regions of comparatively weak cyclonic flow and three weak radial arms. Towards the bore, $r/b \leqslant 0.25$, the flow is virtually axisymmetric. In frame (e), where the discs are heated with distribution D and the shroud is also heated, the flow inside the cavity appears to have broken down into a number of streams. These flow radially outward and radially inward, supplying and collecting fluid into and from the boundary layer on the heated shroud. Adjacent to the shroud, fluid is moving faster than the cavity—presumably as a consequence of its density being reduced by heating and maintaining conservation of angular momentum. As in frame (d), near to the bore, the flow becomes almost axisymmetric.

As previously noted, the flow visualization work of Farthing *et al.*[2] focused on disc surface temperature distributions A and B. The numerical results presented here have shown that under these conditions the flow may commute from having a single radial arm etc., to a pair of radial arms etc. This sensitivity of the flow structure to the imposed surface temperature distribution may serve to explain differences in the observed experimental flows, where in some cases there would be one radial arm and in others two. It is further worth commenting that Farthing[16] carried out some flow visualization work with a heated shroud and noted the existence of 'multiple radial arms' which is not at all inconsistent with the flow illustrated in *Figure 7e*.

Comparison between numerical predictions and experimental flow visualization

Much of the experimental evidence of the flow structure has been obtained from flow visualization. (Atomized oil particles are injected into the central throughflow and a collimated

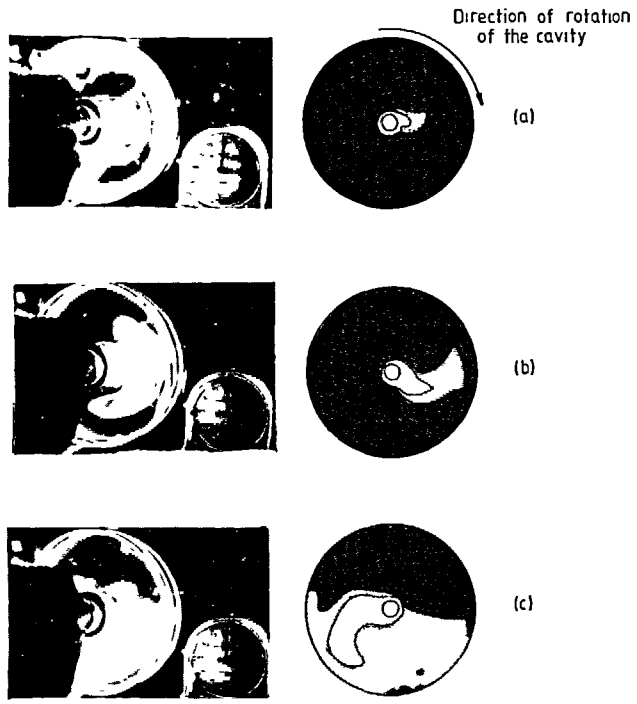

Figure 8 Comparisons between flow visualization results and numerical predictions ($Sc = \infty$ and for disc surface temperature distribution A); for $Re_\phi = 1.3 \times 10^4$, $Re_z = 2180$ and $G = 0.267$. (a) $t = 1$; (b) $t = 3$; (c) $t = 7$ sec

sheet of Laser light illuminates either an r–θ or r–z plane inside the cavity.) The governing equation for the transport of a species is given by (4). The velocities in the convective terms of (4), $w\partial C/\partial z$ etc., were obtained from the predicted velocity field (obtained from solving (2) and (3)). It was not possible to obtain precise information on the diffusive properties of the oil particles in the air. However, since the motion of the oil particles will be governed by Stokes' law, it is considered that setting the diffusion coefficient, Γ, in (4) to zero, should give a good description of their motion.

A comparison between the numerical (with temperature distribution A and $Sc = \nu/\Gamma$, $= \infty$) and experimentally observed flow structures is given in *Figure 8*. The experimental results were obtained using a high speed video camera (Kodak Ektapro); the areas of white are where atomized smoke particles are illuminated by a collimated sheet of laser light, and the cavity is rotating in a clockwise sense. The numerical results simulate the concentration of atomized smoke droplets in the cavity at the same time as recorded in the experiment: frame (a) at 1 sec from when the smoke first appeared in the cavity, (b) at 3 sec and (c) at 7 sec. The sense of rotation is the same as in the experiment, and the grey scale chosen attempts to match that in the experimental results. In frame (a) both the numerical and experimental results show the radial arm. In frame (b) this bifurcates and begins to form the cyclonic and anticyclonic regions which are evident in frame (c).

The velocity field in the cavity

The following discussion and graphs of velocity profiles were obtained using disc surface temperature distribution B. This was chosen as it is considered to strike a balance between

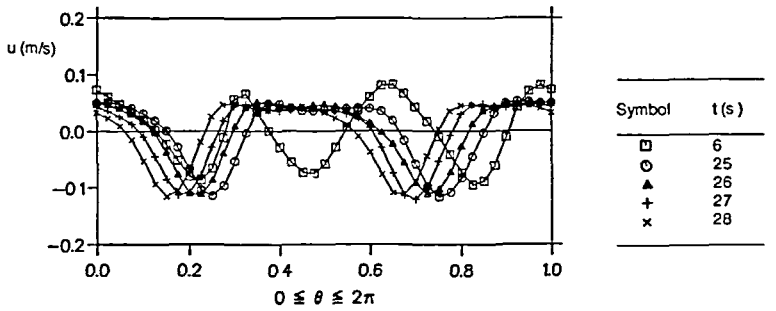

Figure 9 Circumferential variation of radial velocity at different times at $z/s = 0.5, r/b = 0.6$; for temperature distribution B, a parabolic inlet velocity profile, $Re_\phi = 1.3 \times 10^4$ and $Re_z = 2180$

showing the essential features of the flow and simplicity (the flow structure for this distribution always has two radial arms and does not commute). *Figure 9* shows the circumferential variation of radial velocity, u, at $z/s = 0.5$ and $r/b = 0.6$ for disc surface temperature distribution B, a parabolic inlet velocity profile and at a number of different times ($t = 6, 25, 26, 27$ and 28 sec).

The angle, θ, is taken as being positive in an anticlockwise direction from the '3 o'clock position'. A negative value of u indicates that the fluid moves radially inward, conversely the flow moves radially outward when $u > 0$. The velocity profile for $t = 6$ sec is distinctly different to the others indicating that at this time the flow is still developing with time and the cyclic nature of the flow is not yet established. For $t \geqslant 25$ sec, where the flow is cyclic, the curves are similar and there is a shift ($1 - \omega/\Omega = 0.01$) indicating that there is relative tangential motion of the fluid inside the cavity. For the value of Re_z considered here ($Re_z = 2180$) the bulk average velocity of the central throughflow, W, is 1.5 m/sec; the computed radial velocities are shown to generally be an order of magnitude lower than this. At $r/b = 0.6$, radial outflow occupies a larger sector than radial inflow (which can also be seen in the velocity vector plots shown in *Figure 7b*). However, the greatest peak velocities occur when the flow moves radially inward.

The circumferential variation of radial velocity obtained using a uniform velocity distribution at inlet, at three axial locations: $z/s = 0.02$, 0.5 and 0.98 ($z/s = 0$ corresponds to the upstream disc and $z/s = 1$ the downstream disc) is shown in *Figures 10a, b* and *c*, respectively. Each frame shows the results at three different radial locations: $r/b = 0.2$, 0.6 and 0.9 and the plots are obtained for $t = 30.9$ sec. The three diagrams indicate the complex nature of the flow; generally a quadrant in any r–θ plane can have both outflow and inflow. The magnitude of the velocities is generally greater away from the outer part of the cavity. This presumably occurs due to the decrease in cross-sectioual area with decreasing radial coordinate. It is interesting to compare the results for $z/s = 0.02$ and 0.98 equal distances from the upstream and downstream discs, respectively. For $r/b = 0.6$ and 0.9 there is little difference in the results but there are significant differences at $r/b = 0.2$. In particular, where there is radial outflow, the velocities are greater adjacent to the downstream disc (at $z/s = 0.98$)—presumably due to the action of the central throughflow itself. When there is radially-inward flow, the velocities at all three axial locations for $r/b = 0.2$ are similar. Further examination reveals that at $r/b = 0.2$, radial inflow occurs in two distinct sectors, at about $\theta = 0.6\pi$ and $\theta = 1.6\pi$, with the least amount of fluid flowing radially inward adjacent to the downstream disc. Comparison between *Figure 10b* for $r/b = 0.6$, and the results shown in *Figure 9* illustrates that the assumed velocity profile at inlet has little influence on the flow well into the cavity. *Figure 11* shows the axial variation of tangential velocity, v, computed using a uniform velocity profile at inlet, at $r/b = 0.2$, 0.6 and 0.9 for different circumferential locations and at $t = 30.9$ sec. A positive value of v indicates that the tangential velocity of the flow exceeds that of the discs, the converse applies when v is negative. For $r/b = 0.6$ and 0.9 the axial variation of tangential velocity is virtually symmetrical about

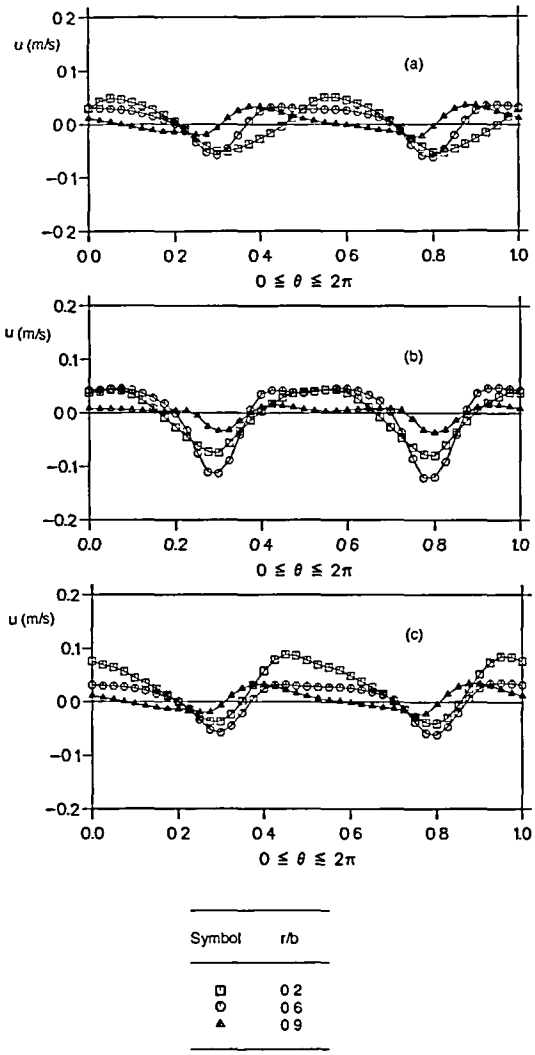

Figure 10 Circumferential variation of radial velocity at different radii; for temperature distribution B at 30.9 sec, a uniform inlet velocity profile, $Re_\phi = 1.3 \times 10^4$ and $Re_z = 2180$. (a) $z/s = 0.02$; (b) $z/s = 0.5$; (c) $z/s = 0.98$

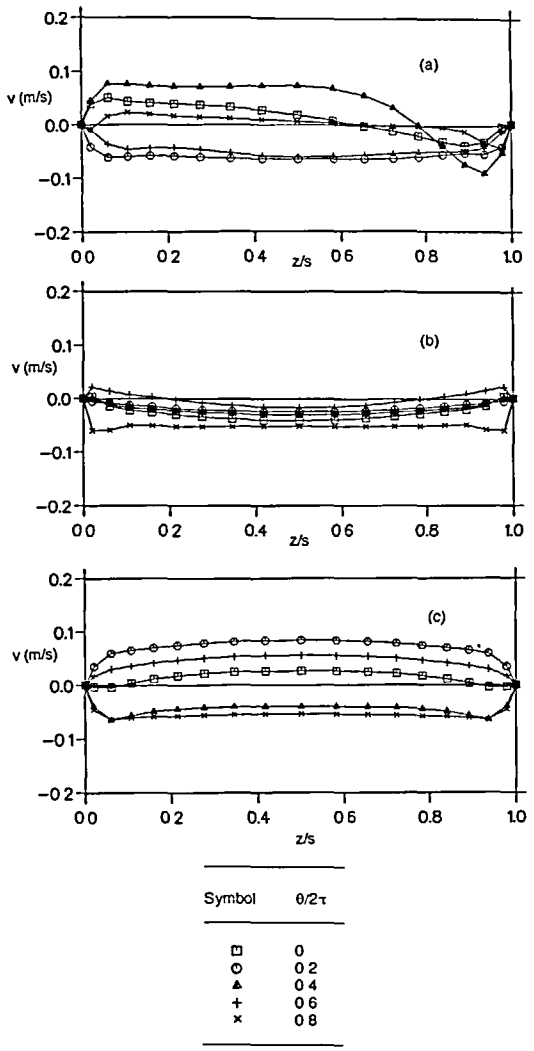

Figure 11 Axial variation of tangential velocity at different circumferential locations; for temperature distribution B at 30.9 sec, a uniform inlet velocity profile, $Re_\phi = 1.3 \times 10^4$ and $Re_z = 2180$. (a) $r/b = 0.2$; (b) $r/b = 0.6$; (c) $r/b = 0.9$

the mid-axial plane but not at $r/b = 0.2$. There appear to be regions close to each disc where there is a relatively large change in v, indicating the existence of boundary layers. Between these regions, there is little change in v with axial location. Comparing the results for the different circumferential locations shows that there is both cyclonic $v > 0$ and anticyclonic flow $v < 0$ at the same radial location.

The axial variations of radial velocity (at $t = 30.9$ sec and with a uniform inlet velocity profile) are shown in *Figures 12a, b* and *c* for $r/b = 0.2$, 0.6 and 0.9, respectively. As was noted for the tangential velocity, there is here also a region close to the surface of each disc where the radial velocity varies significantly. As also noted in *Figure 10*, at any radial location there is both radial

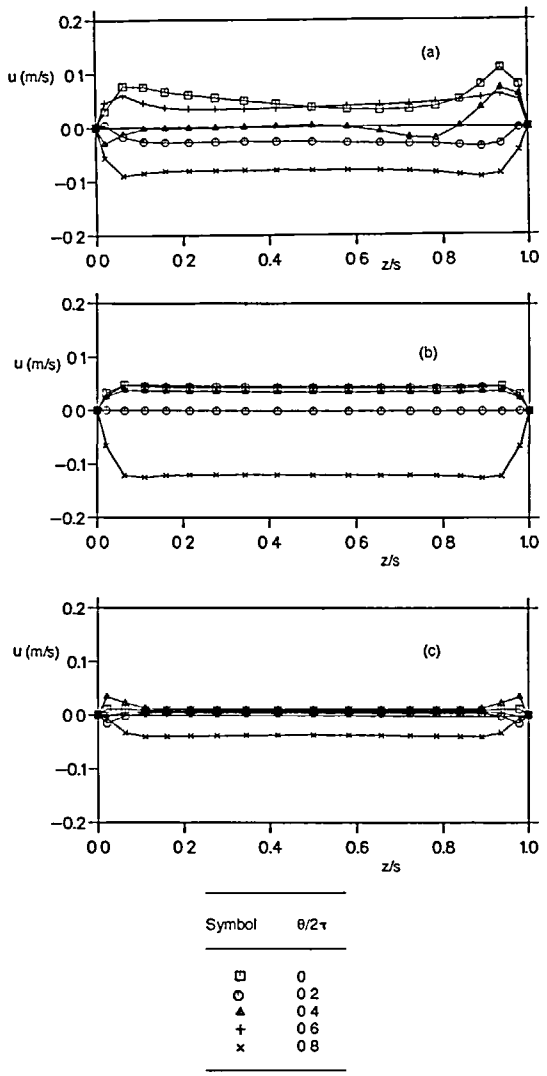

Figure 12 Axial variation of radial velocity at different circumferential locations; for temperature distribution B at 30.9 sec, a uniform inlet velocity profile, $Re_\phi = 1.3 \times 10^4$ and $Re_z = 2180$. (a) $r/b = 0.2$; (b) $r/b = 0.6$; (c) $r/b = 0.9$

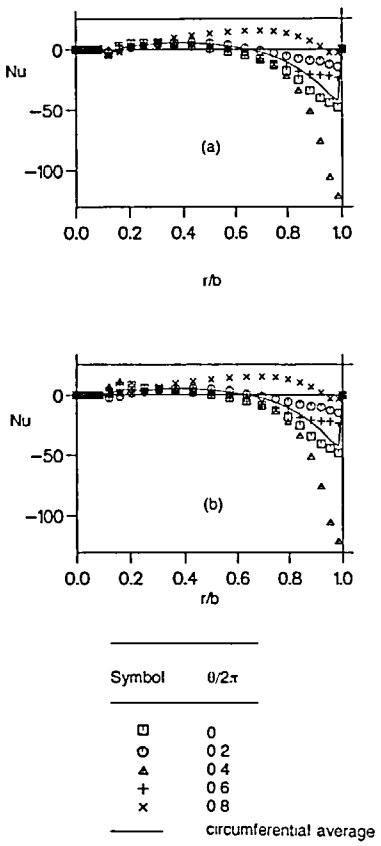

Figure 13 Radial variation of local Nusselt number at different circumferential locations; for temperature distribution B at 30.9 sec, a uniform inlet velocity profile, $Re_\phi = 1.3 \times 10^4$ and $Re_z = 2180$. (a) Upstream disc and (b) downstream disc

inflow and outflow and as shown in the velocity vector plots (*Figure 7b*), these regions are separated by regions of cyclonic and anticyclonic flow. For $r/b = 0.6$ and 0.9 the axial variation of radial velocity is virtually symmetrical about the mid-axial plane, this does not occur at $r/b = 0.2$ due to (as noted above) the influence of the central throughflow which appears to create some recirculation adjacent to the downstream disc. At $r/b = 0.9$ the flow is comparatively weak which is consistent with experimental observations. The magnitudes of the relative-tangential and radial velocities are comparable at $r/b = 0.2$ (cf. *Figures 11a* and *12a*). At $r/b = 0.6$, the radial velocity exceeds the relative-tangential velocity and at $r/b = 0.9$ the relative-tangential velocity exceeds the radial velocity.

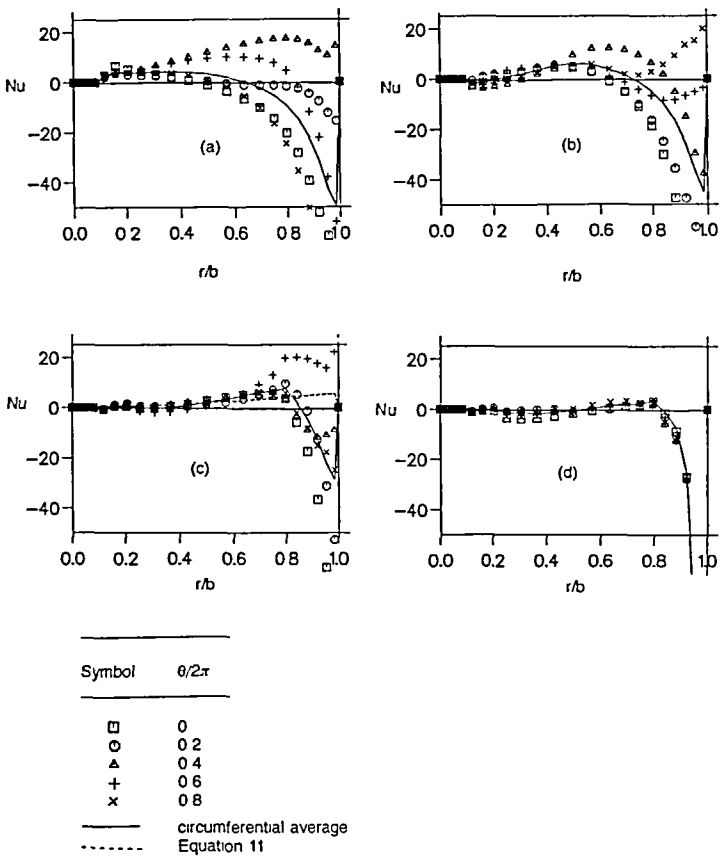

Figure 14 Radial variation of local Nusselt number at different circumferential locations on the upstream, disc and for different temperature distributions; for a uniform inlet velocity profile, $Re_\phi = 1.3 \times 10^4$ and $Re_z = 2180$. (a) Distribution A, $t = 60$ sec; (b) distribution C, $t = 33$ sec; (c) distribution D, $t = 59$ sec; (d) distribution D and a heated shroud, $t = 88.6$ sec

Nusselt number distributions

Figures 13a and *b* show the radial variation of local Nusselt number, Nu (defined using $L = r$) for disc surface temperature distribution B and at $z/s = 0$ and $z/s = 1$ corresponding to the upstream and downstream disc faces, respectively. The results are shown for a value of $t = 30.9$ sec and at five different circumferential locations. For $r/b > 0.3$, the results for each disc are virtually identical. For $r/b < 0.3$ the differences between the upstream and downstream discs are attributed to the recirculation effect noted above. There are circumferential variations in the Nusselt number but the circumferentially-averaged value decreases with increasing radius. The experimental results[1] for a similar surface temperature distribution were obtained at larger values of rotational and axial Reynolds numbers than these numerical results. But it is encouraging to note that, the radial distribution of local Nusselt numbers seen here is consistent with their experimental work.

The effect of disc surface temperature distribution on the computed Nusselt numbers from the upstream disc is shown in *Figure 14*. These results were obtained at the same times as the vector plots shown in *Figure 7*. As the radial location of the maximum disc surface temperature moves outward (distributions A to D) the circumferentially-averaged Nusselt number becomes

less negative. There is also a damping down of the circumferential variation in Nusselt number, presumably because the flow structure itself tends to become more axisymmetric. The heat transfer towards the outer radius is always negative, i.e., into the disc. This occurs because the disc temperature here is set to the fluid inlet temperature. When the shroud is heated, this increases the heat transfer into the disc surface at the outer radius, because the fluid now receives additional heat from the shroud. The results shown in frame (c) are for surface temperature distribution D, which is similar to that used to obtain a correlation of the heat transfer by Farthing *et al.*[1] This is also shown on the graph and in the current nomenclature is given by:

$$Nu = 0.0054 Re_z^{0.3} Re_\phi^{1/2} \beta \Delta T^{1/4} (r/b)((b/r) - 1)^{-1/4} \quad (11)$$

The numerical results in *Figure 14c* are for $r/b \leqslant 0.8$ in reasonable accord with this correlation. The discrepancy at $r/b > 0.8$ is attributed to a difference between the boundary condition assumed here for the shroud (at $T = T_i$) and that in the experiments (adiabatic).

CONCLUSIONS

Numerical results are presented in this paper for the heated flow structure in a rotating cavity with an axial throughflow of cooling air. The results are shown for $Re_\phi = 1.3 \times 10^4$, $Re_z = 2180$ and five different surface temperature distributions are investigated. The time-dependent three-dimensional form of the equations of continuity, momentum and energy are solved in a coordinate system rotating at the angular speed of the cavity. Laminar flow is considered and the governing equations are solved using a finite volume formulation and a multigrid technique.

The flow structure is three-dimensional and is seen to exhibit a cyclic form of time dependence. The predicted flow structure is consistent with experimental results obtained using laser-illuminated flow visualization. Flow is seen to enter the cavity in radial arms, flanked by regions of cyclonic and anticyclonic circulation. Where there are regions of cyclonic flow, fluid moves axially away from the disc surface, for regions of anticyclonic flow, the converse applies. The separation region reported in the experimental work, although present is not a permanent feature of the flow in the numerical results—and currently no reason is suggested for this discrepancy.

As noted experimentally, the flow and heat transfer depends most strongly on the disc surface temperature distribution. For an unheated peripheral shroud, the number of radial arms, cyclonic and anticyclonic recirculation regions increases (from 1, to 2, to 3) as the location of the maximum disc surface temperature moves radially outward. When the shroud is also heated, there are many (>4) radial arms which appear to exchange fluid with the boundary layer on the shroud.

For surface temperature distribution B (investigated in some detail), the predicted relative-tangential and radial velocities are found to be an order of magnitude less than the bulk average velocity of the axial throughflow. The axial and circumferential variations of relative-tangential and radial velocity indicate a complex flow structure inside the cavity. Boundary layers form on the discs, and for a given radial location there are sectors where the flow moves radially inward and sectors where the flow is radially outward. In the centre of the cavity the flow can also be either radially inward or radially outward. Away from the axis of rotation the flow is virtually symmetrical about the mid-axial plane; close to the axis there is asymmetry due to the influence of recirculation adjacent to the downstream disc.

There is also a strong effect of the disc surface temperature distribution on the local Nusselt numbers. As the location of the maximum disc temperature moves radially outward the circumferentially-averaged Nusselt numbers become less negative. There is also a reduction in the circumferential variation of Nu, because the flow structure itself tends to become more axisymmetric. There is reasonable agreement between correlated and predicted Nusselt numbers for a surface temperature distribution similar (but not identical) to that used in experimental work to obtain a correlation. The recirculation of fluid adjacent to the downstream disc causes some enhancement of the heat transfer towards the inner radius of this disc.

ACKNOWLEDGEMENTS

Some of the computations were carried out on The Science and Engineering Research Council's Cray XMP at the Rutherford Appleton laboratory. The authors also wish to thank Dr. Craig Vaughan for his efforts in the 'early days' of this research. Finally, we extend our appreciation to Rolls-Royce plc and SERC for funding this research.

REFERENCES

1 Farthing, P. R., Long, C. A., Owen, J. M. and Pincombe, J. R. Rotating cavity with axial throughflow of cooling air: heat transfer, *ASME J. Turbomach.*, **114**, 229 (1992)
2 Farthing, P. R., Long, C. A., Owen, J. M. and Pincombe, J. R. Rotating cavity with axial throughflow of cooling air: flow structure, *ASME J. Turbomach.*, **114**, 237 (1992)
3 Tucker, P. G. Numerical and experimental investigation of flow structure and heat transfer in a rotating cavity with an axial throughflow of cooling air, *DPhil. Thesis*, School of Engineering, University of Sussex (1993)
4 Patankar, S. V. *Numerical Heat Transfer and Fluid Flow*, Hemisphere, New York (1980)
5 Spalding, D. B. A novel finite-difference formulation for differential expressions involving both first and second derivatives, *Int. J. Num. Meth. Eng.*, **4**, 551 (1972)
6 Van Doormal, J. P. and Raithby, G. D. Enhancement of the SIMPLE method for predicting incompressible fluid flows, *Num. Heat Transfer*, **7**, 147 (1984)
7 Gosman, A. D., Koosinlin, M. L., Lockwood, F. C. and Spalding, D. B. Transfer of heat in rotating systems, *ASME Paper 76-GT-25* (1976)
8 Vaughan, C. M. A numerical investigation into the effect of an external flow field on the sealing of a rotor-stator cavity, *DPhil Thesis*, School of Engineering, University of Sussex (1987)
9 Vaughan, C. M., Gilham, S. and Chew, J. W. Numerical solutions of rotating disc flows using a non-linear multigrid algorithm, *Proc. 5th Int. Conf. Num. Meth. Lam. and Turb. Flow*, Pineridge Press, Swansea, p. 63 (1989)
10 Bontoux, P., Smutex, C., Roux, B. and Lacroix, J. M. Three dimensional buoyancy-driven flows in cylindrical cavities with differentially heated end walls. Part 1. Horizontal cylinders, *Int. J. Heat Mass Transfer*, **169**, 21 (1986)
11 Schiroky, G. H. and Rosenberger, F. Free convection of gases in a horizontal cylinder with differentially heated end walls, *Int. J. Heat Mass Transfer*, **27**, 587 (1984)
12 Castrejon, A. and Spalding, D. B. An experimental and theoretical study of transient free convection flow between horizontal concentric cylinders, *Int. J. Heat Mass Transfer*, **31**, 273 (1988)
13 Hide, R. An experimental study of thermal convection in a rotating liquid, *Phil. Trans.* (*A*), **250**, 441 (1958)
14 Hignett, P., White, A. A., Carter, R. D., Jackson, W. D. N. and Small, R. M. A comparison of laboratory measurements and numerical simulations of baroclinic wave flows in a rotating cylindrical annulus, *Q. J. R. Met. Soc.*, **111**, 131 (1985)
15 White, A. A. personal communication (1992)
16 Farthing, P. R. The effect of geometry on flow and heat transfer in a rotating cavity, *DPhil Thesis*, School of Engineering and Applied Sciences, University of Sussex (1988)